

Accepted Article

Title: Deciphering the Factors Controlling Hydrogen and Methyl Spillover on Rh/Cu(111) Single-Atom Alloy

Authors: Kaixuan Gu, Hua Guo, and Sen Lin

This manuscript has been accepted after peer review and appears as an Accepted Article online prior to editing, proofing, and formal publication of the final Version of Record (VoR). The VoR will be published online in Early View as soon as possible and may be different to this Accepted Article as a result of editing. Readers should obtain the VoR from the journal website shown below when it is published to ensure accuracy of information. The authors are responsible for the content of this Accepted Article.

To be cited as: Angew. Chem. Int. Ed. 2024, e202405371

Link to VoR: https://doi.org/10.1002/anie.202405371

Deciphering the Factors Controlling Hydrogen and Methyl Spillover upon Methane Dissociation on Rh/Cu(111) Single-Atom Alloy

Kaixuan Gu, a,b Hua Guo, c,* and Sen Lina,*

^aState Key Laboratory of Photocatalysis on Energy and Environment, College of

Chemistry, Fuzhou University, Fuzhou 350002, China

^bCollege of Chemistry and Molecular Sciences, Henan University, Kaifeng 475001,

China

^cDepartment of Chemistry and Chemical Biology, Center for Computational Chemistry, University of New Mexico, Albuquerque, New Mexico, 87131, USA

^{*:} Corresponding authors: hguo@unm.edu and slin@fzu.edu.cn

Abstract Spillover of adsorbed species from one active site to another is a key step in heterogeneous catalysis. However, the factors controlling this step, particularly the spillover of polyatomic species, have rarely been studied. Herein, we investigate the spillover dynamics of H* and CH₃* species on a single-atom alloy surface (Rh/Cu(111)) upon the dissociative chemisorption of methane (CH₄), using molecular dynamics that considers both surface phonons and electron-hole pairs. These dynamical calculations are made possible by a high-dimensional potential energy surface machine learned from density functional theory data. Our results provide compelling evidence that the H* and CH₃* can spill over on the metal surface at experimental temperatures and reveal novel dynamical features involving an internal motion during diffusion for CH₃*. Increasing surface temperature has a minor effect on promoting spillover, as geminate recombinative desorption becomes more prevalent. However, the poisoning of the active site can be mitigated by the frequent gaseous molecular collisions that occur under ambient pressure in real-world catalysis, which transfer energy to the trapped adsorbates. Interestingly, the bulky CH₃* exhibits a significant spillover advantage over the light H* due to its larger size, which facilitates energy acquisition. These insights help to advance our understanding of spillover in heterogeneous catalysis.

Keywords: Gaseous molecular collisions; spillover; machine learning; potential energy surface; molecular dynamics

Introduction

Single-atom alloys (SAAs) represent a promising class of single-site catalysts where isolated metal atoms are dispersed in the surface layer of a metal host^[1]. This new concept has found extensive applications in various heterogeneous catalytic processes^[2]. Typically, the atomically dispersed dopant is an active metal for the initial dissociative chemisorption of an impinging molecule^[3]. while the host helps to catalyze subsequent steps involving the chemisorbed dissociation products^[4]. In the case of selective alkene hydrogenation catalyzed by platinum group metal dopped Cu(111) SAA catalysts^[3c, 4a-c], for example, the initial H₂ dissociative chemisorption happens exclusively at the Pd/Pt site with a low barrier, while the hydrogen addition of alkene double bonds occurs at Cu sites. Importantly, the catalytic performance of the SAAs is closely related to spillover, a phenomenon that refers to the migration of dissociated fragments of the impinging molecules from the dissociation site to other sites on the surface^[5]. Spillover is not only important for the formation of the target product on the host surface, but also key in preventing undesired side processes such as coking [3d, 4b, 4d, ⁶]. For many SAAs, the high activity of the dopant site often leads to strong binding affinities for dissociation products, which could inhibit spillover^[3a, 3e, 7].

Fundamentally, the migration of translationally "hot" adsorbates depends not only on the potential landscape such as the barriers for dissociation and diffusion^[3a, 6b, 6c, 8], but more importantly on the dynamics and energy exchange between the dissociation fragments and the surface^[9]. Under ambient pressure conditions in real-world heterogeneous catalysis, spillover can also be affected by collisions between molecules

from the gas phase and the adsorbed species, allowing the latter to acquire the additional energy necessary to overcome the diffusion energy barrier^[10]. Consequently, the dynamics of spillover on SAAs need to be fully understood.

Unfortunately, direct observations of the transient evolution of spillover are extremely challenging in experiments, making it hard to gain quantitative insights. In theoretical calculations, an in-depth study of the intricate dynamics of spillover requires molecular dynamics (MD) simulations with a first-principles characterization of the interaction potential. This often requires a large number of trajectories and extensive propagation times for such a low-probability and long process in order to obtain reliable statistical results^[11], which is a significant challenge in terms of computational cost. Currently, an emerging approach is to take advantage of machine learning to construct accurate and efficient potential energy surfaces (PESs) to accelerate MD calculations^[12]. With the aid of first-principles based PESs, our recent theoretical studies have significantly advanced our understanding of hydrogen (H*) spillover on the Pt/Cu(111) SAA^[9c, 9d, 10].

Here, we present comprehensive dynamic insights into the spillover processes of both atomic hydrogen (H*) and polyatomic methyl (CH₃*) upon methane (CH₄) dissociation on a Rh/Cu(111) SAA surface. As reported by Sykes and co-workers, [4d] Rh/Cu(111) SAA surfaces exhibit remarkable thermodynamic stability and high activity for CH₄ dissociation, while retaining considerable coke resistance. To quantitatively characterize the initial dissociation and subsequent spillover dynamics, we employed an uncertainty-driven active learning strategy to construct a high-dimensional neural

network PES, on which extensive MD simulations with and without electron-hole pairs (EHPs) were performed. The simulation of spillover of polyatomic species has not been reported before and we show in this work novel dynamical features involving the internal motion during diffusion. More importantly, our atomistic simulation results provide compelling evidence that H* and CH₃* are capable of spilling over from the Rh site to the Cu site upon CH₄ dissociation and then undergo extensive thermal diffusion on the host Cu(111) surface at experimental temperatures. Interestingly, our results suggest that heating the surface does not necessarily help spillover, as the chances for nascent H* and CH3* to recombine into CH4 molecules increases with temperature. Furthermore, our simulations revealed that collisions of gas-phase CH₄ molecules with the surface, which are prevalent under ambient pressure conditions, help to drive the H* or CH₃* to spill over onto the host Cu. For such collision induced spillover events, CH₃* has a significant advantage over H* due to its larger size, which favors energy transfer. These results provide valuable insights into spillover mechanisms and dynamics on an atomic scale, which may assist in the future design of new SAA catalysts. The investigation of gas-surface collision-induced effects on surface processes also helps to bridge the pressure gap between surface science and real-world heterogeneous catalysis.

Results and Discussion

The static reaction pathways of CH₄ dissociation and the subsequent diffusion of H* or CH₃* on the Rh/Cu(111) surface computed by DFT are depicted in Figure 1, with energies and geometries of relevant stationary points. For the dissociation, gaseous CH₄

initially enters a physisorption well (-0.216 eV) atop the Rh atom (MIN1). The center of mass of CH₄, which has a geometry close to its gas phase equilibrium, is located at a height (Z) of 3.07 Å above the surface plane. The dissociation saddle point (SP1) adopts a configuration at the top of the Rh atom with a significantly elongated C-H distance of 1.62 Å and a reduced Z = 2.41 Å. In the final state (MIN2), the dissociated H* and CH₃* species occupy Cu-Rh-Cu hollow sites on the opposite ends of the Rh site. The barrier of CH₄ dissociation at the Rh site on the Rh/Cu(111) surface is calculated to be 0.554 eV related to the gas-surface asymptote, which is in good agreement with previous calculations for this system (~0.53 eV)^[4d]. This barrier is much lower than that on Cu(111), which is 1.30 eV^[4d].

As shown in the upper panel of Figure 1, the MIN2 structure is quite stable and the energy barrier for H* to diffuse to an adjacent Cu-Cu-Cu hollow site (MIN3) is 0.332 eV. On the other hand, further H* diffusion is much easier as the energy barrier to the next Cu-Cu-Cu hollow site (MIN4) is merely 0.045 eV. The hcp site (MIN4) is slightly more stable than the fcc site (MIN3) and the inverse barrier from MIN4 to MIN3 is 0.155 eV, resembling the barrier for H diffusion on the neat Cu(111) surface (~0.14 eV)^[13].

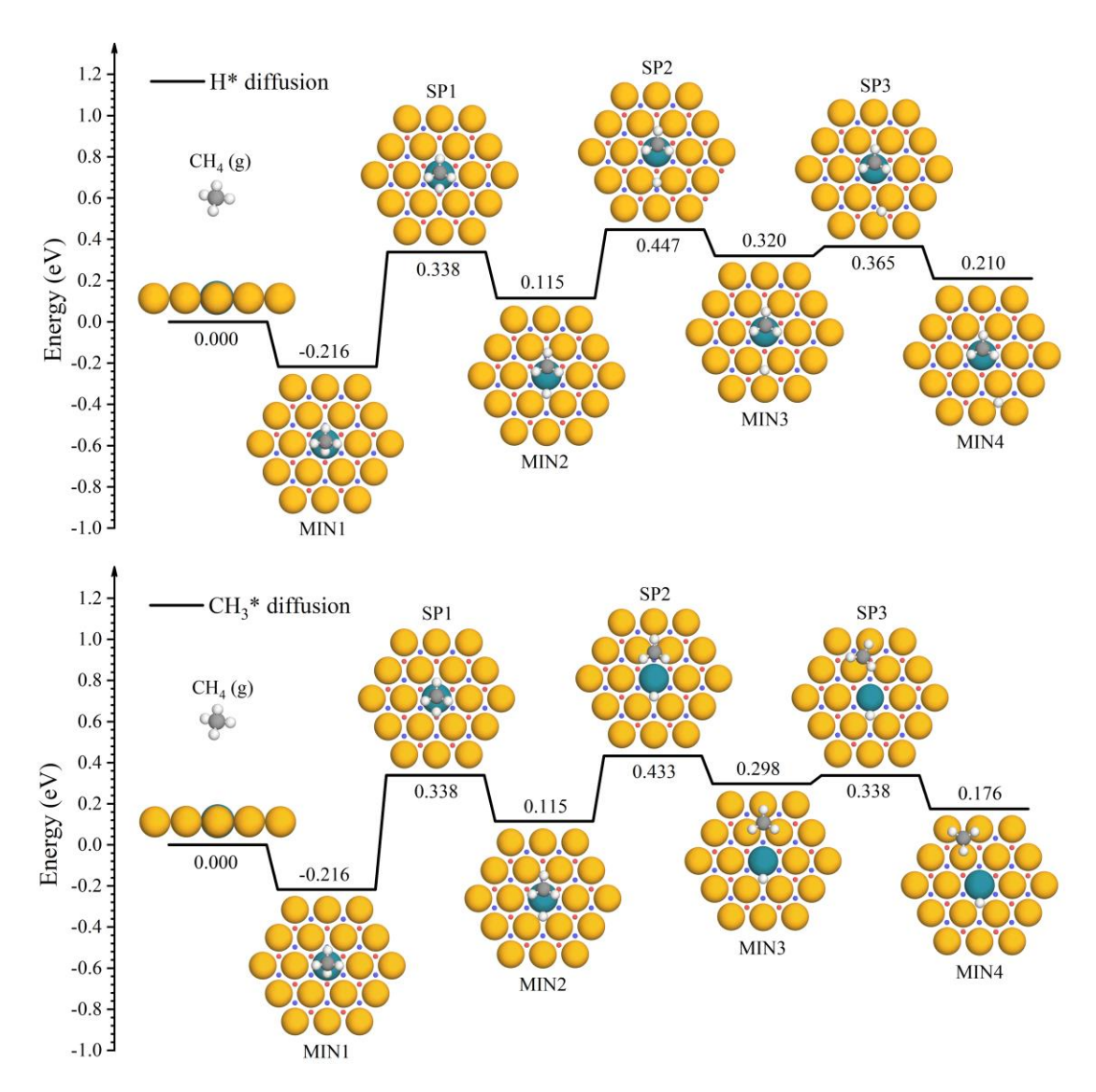


Figure 1. Energy profiles for CH₄ dissociation and H* (upper panel) or CH₃* diffusion (lower panel) on the Rh/Cu(111) surface. Stable adsorption configurations for the CH₄ molecule, H* and CH₃* denoted by potential minima (MIN) and the saddle points (SP) between the minima are presented in the Figure. The energy zero is defined for CH₄ far above the surface. White, grey, orange, and cyan spheres represent H, C, Cu, and Rh atoms, respectively. Small red and blue spheres represent hcp and fcc sites, respectively. For clarity, only the top layer of the Rh/Cu(111) surface is shown.

A similar potential landscape is found for the diffusion of CH₃* on the Rh/Cu(111) surface, as shown in the lower panel of Figure 1. The energy barrier for the CH₃* migration from MIN2 to the adjacent Cu-Cu-Cu hollow site (MIN3) is 0.318 eV.

Further CH₃* diffusion between Cu sites is easier. The calculated barrier is 0.040 eV for diffusion from MIN3 to MIN4, and 0.162 eV for the reverse process. This is consistent with previous calculations for CH₃* diffusion from a hcp site to an fcc site on the Cu(111) surface (\sim 0.05 eV)^[14].

The static energetics in Figure 1 suggests that initial escape of the dissociation products from the Rh site can be difficult due to the relatively large barriers. However, since the dissociation provides kinetic energies to H* and CH₃*, the fate of these nascent species depends on dissociation dynamics and subsequent energy exchange with surface atoms.

An embedded atom neural network (EANN) PES is constructed for CH₄ dissociation on the bare Rh/Cu(111) surface and for CH₄ collisions of an H* and CH₃* adsorbed surface. The EANN employed two hidden layers with 30 and 50 neurons and a cutoff radius of 6 Å. The PES was fitted using 4759 DFT points, consisting of 2455 points from the CH₄+ Rh/Cu(111) system, 495 points from the CH₄+ H*@Rh/Cu(111), 881 points from the CH₄ + CH₃*@Rh/Cu(111), and 928 points from the CH₄ + (H*+CH₃*)@Rh/Cu(111) systems. Both energies and gradients were used in the NN optimization. For training purposes, 90% of the points were utilized, with the remaining 10% allocated for testing. The root-mean-square error (RMSE) for the training/validation set is 18.4/36.5 meV in energy per cell and 31.1/35.4 meV/Å in atomic forces. To assess the accuracy of the EANN PES, the DFT energies along several AIMD trajectories are compared in Figure S1 with the values obtained from the PES, demonstrating a high fidelity of the NN fit. To facilitate the EF calculations, the electron

density surface (EDS)^[15] as a function of cartesian coordinates was represented using the same EANN method from 260 sampled configurations. The RMSE of the EDS is 1.50×10^{-4} e/Å³ indicating that the DFT density was successfully reproduced.

We first examine the dissociation dynamics and the subsequent "hot" adsorbate dynamics on the Rh/Cu(111) surface using the EANN PES. As shown in our previous work^[9c], H* spillover and diffusion on the Pt/Cu(111) SAA surface is strongly influenced by nonadiabatic effects induced by the excitation of EHPs. Hence, we report both the QCT and QCT-EF results.

Several incidence energies and angles for the impinging CH₄ as well as surface temperatures were considered, and the results for a 2 ps simulation are given in Figure 2. Here, the probabilities in the Figure are defined as the number of trajectories for a particular event over the total number of trajectories. A total of 3×10⁴ trajectories were calculated for each set of initial conditions. We note in passing that such a large number of trajectories would be computationally infeasible if the DFT forces were to be computed on the fly, underscoring the advantage of a machine learned PES.

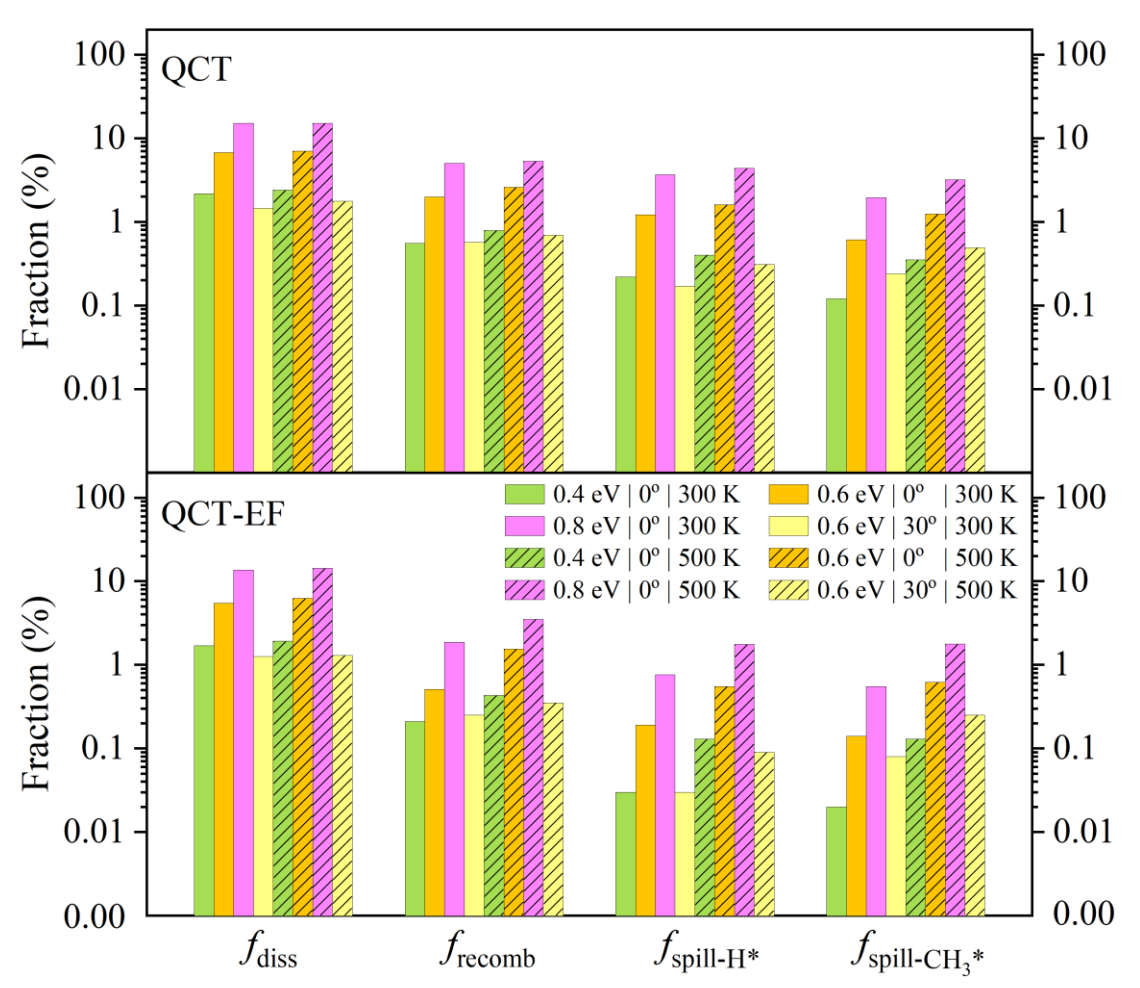


Figure 2. Fractions of CH₄ dissociation (f_{diss}), H* spillover ($f_{spill-H*}$), CH₃* spillover ($f_{spill-CH_3*}$) and CH₄ recombination (f_{recomb}) after CH₄ dissociation, obtained from QCT (upper panel) and QCT-EF (lower panel) calculations with different incident energies (E_i) and incident angles (θ_i) at the surface temperatures of 300 K and 500 K. 3×10^4 QCT-EF trajectories were propagated for each condition with a propagation time of 5 ps.

It is clear from Figure 2 that dissociation probabilities for the impinging CH₄ are small, but increase with incidence energy, consistent with the activated nature of this process. The dissociation is minimally impacted by the EHPs, as evidenced by the similar QCT and QCT-EF values in Figure 2, which is consistent with an earlier study on dissociative chemisorption of CH₄ on Ni (111)^[16]. The incidence angle reduces the kinetic energy in the normal direction, leading to lower dissociation probabilities. In

addition, the influence of the surface temperature is small for dissociation.

The initial spillover of the two dissociation products is not facile, evidenced by the small $f_{\text{spill-H}}$ and $f_{\text{spill-CH3}}$, although they become larger at higher incidence energies. The sluggishness in escaping the initial dissociation site is apparently due to the relatively deep potential wells at MIN1, shown in Figure 1. In most spillover events, only one of the two dissociation products escapes the Rh site, analogous to previous observations for H* spillover following H₂ dissociation on SAA surfaces^[9a, 9c]. The spillover probabilities for H* and CH₃* are quite similar, attributable to the similar initial barriers for the two species shown in Figure 1. These probabilities are significantly reduced when the EHPs are introduced, which exert a drag on the adsorbed species. This is consistent with our previous observations for H* spillover^[9c], but the strong EF effect on CH₃* diffusion has not been reported before. On the other hand, the surface temperature seems to promote the spillover. An interesting observation is that CH₃* spillover seems to be more favored for the incident angle of 30°.

Some dissociation fragments undergo geminate recombinative desorption and the probability is typically larger than spillover. This is consistent with the lower energy barrier (0.223 eV) for CH₄ recombination than that of H* spillover (0.332 eV) or CH₃* spillover (0.318 eV), as shown in Figure 1. The fraction of CH₄ recombination also increases with the surface temperature, a trend consistent with the observations from the Temperature-Programmed Desorption (TPD) experiments conducted for CH₄ desorption on Rh/Cu(111) SAA catalysts^[4d].

To gain insight into the longer time thermal diffusion, we propagated 1×10⁵ additional 50 ps QCT-EF trajectories at two surface temperatures with an incident energy of 0.6 eV at normal incidence. Compared with Figure S2, where the QCT data are shown, the EHPs have apparently a significant impact on the long-time dynamics of both H* and CH₃*. While the nonadiabatic friction is known for H* diffusion, the large effect of EHPs on CH₃* diffusion is reported here for the first time.

The mean square diffusion distances, $\langle |\Delta r(\Delta t)|^2 \rangle$, for H* and CH₃* were calculated and shown in Figure 3 as a function of time. In the first 10 ps, the slopes of the curves are time dependent and much steeper than those at a longer time, due apparently to the initial impulsive diffusion. After 20 ps, the slopes of the curves become constant, suggesting thermal equilibration. The thermal diffusion coefficient (D) can thus be obtained according to the Einstein's equation^[17]:

$$D = \lim_{\Delta t \to \infty} \frac{\langle |\Delta r(\Delta t)|^2 \rangle}{2d\Delta t} , \qquad (4)$$

where Δt is the diffusion time and d represents the dimension of the system in which diffusion is considered (2 for surface diffusion). The RMSE of D is determined based on the time-dependent diffusion coefficients (D(t)), which are calculated using the data after 30 ps as the validation set according to Einstein's equation:

$$D(t) = \frac{\langle |\Delta r(t)|^2 \rangle - \langle |\Delta r(t_0)|^2 \rangle}{2d(t - t_0)}$$
 (5)

where the time zero t_0 is set at 20 ps to exclude the effects of the initial impulsive diffusion. The D with RMSE for both H* and CH₃* are shown in Figure 3. Specifically, the D of H* at 300 K is $(1.47\pm0.20)\times10^{-5}$ cm²/s, which is in good agreement with our earlier report of $(1.7\pm0.10)\times10^{-5}$ cm²/s on Pt/Cu(111)^[9d].

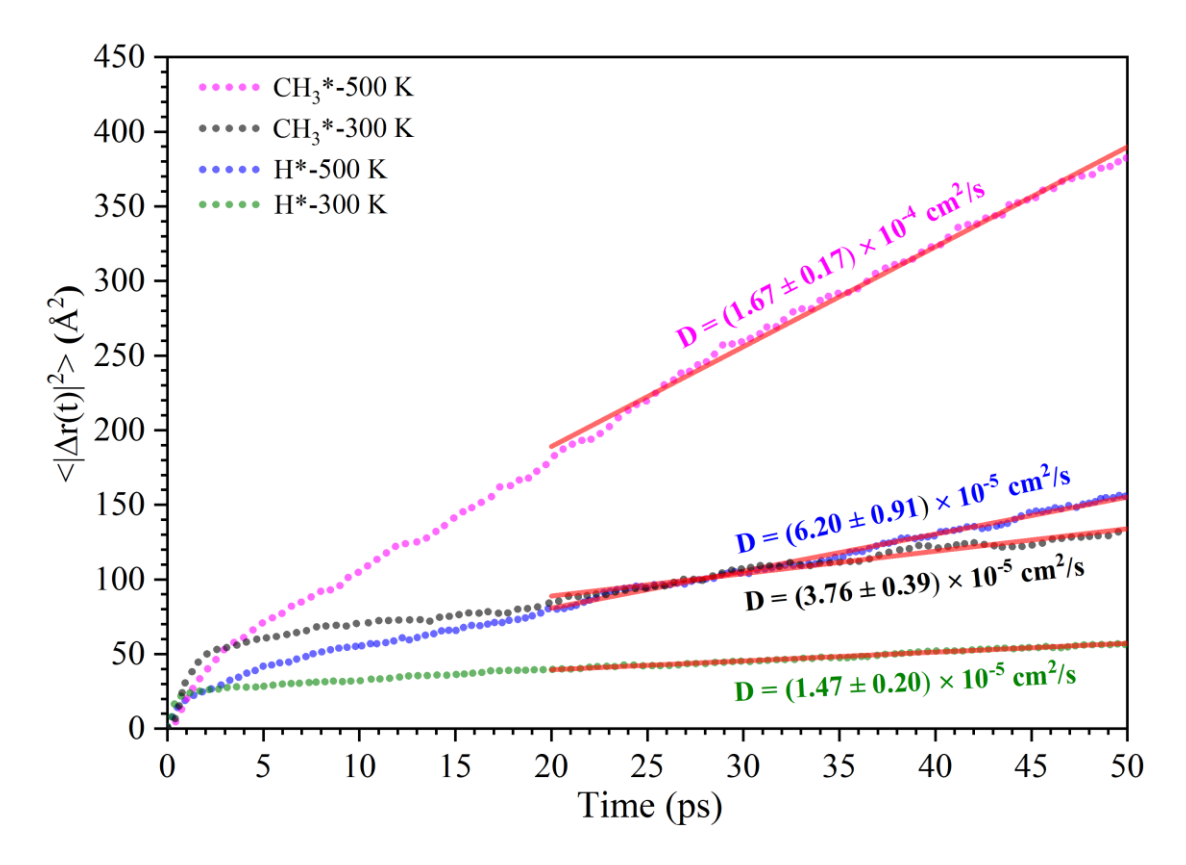


Figure 3. Mean square diffusion distances ($< |\Delta r(t)|^2 >$) and the corresponding diffusion coefficients (D) with RMSEs for the trajectories of H* and CH₃* diffusion as a function of time calculated by the QCT-EF method at the surface temperatures of 300 and 500 K. The fittings are represented by the red straight lines.

Interestingly, at both 300 and 500 K, CH₃* has a larger *D* than that of H*, despite similar diffusion barriers as shown in Figure 1. Analysis of trajectories revealed that directional pseudo-rotation of the CH₃* is involved in diffusion and such an internal motion seems to impart a specific directional preference to its diffusion, in sharp contrast to the random walk diffusion of H*. To understand this phenomenon, we resort to the Sudden Vector Projection (SVP) model^[18], in which reaction coordinate vector at the diffusion transition state is projected onto various modes of the adsorbate. As shown in Table S1, the pseudo-rotational mode of CH₃* is found to strongly coupled with the

reaction coordinate, as shown in Figure S3, explaining the correlation. We note in passing tunneling is not an important factor in H* diffusion at the surface temperatures investigated in this work, as discussed in our previous work^[9c, 9d, 19].

It is clear from the discussion above, spillover of H* and CH₃* is viable, but not very efficient. This can be appreciated by the fact that the energy release from the dissociation barrier is relatively small (0.223 eV), which is often insufficient for the products to overcome the initial barriers from the initial Rh site to an adjacent Cu site $(0.318 \text{ eV for H}^* \text{ and } 0.332 \text{ eV for CH}_3^*)$. Using the EANN PES, we performed 1×10^4 QCT-EF trajectories for impinging CH₄ on three different surfaces: H*@Rh/Cu(111), CH₃*@Rh/Cu(111) and (H* + CH₃*)@Rh/Cu(111). The trajectories were prepared using the same initial conditions as discussed in Methods, and propagated for 5 ps. The initial distributions of H*, CH3*, co-adsorbed H* and CH3* at the Rh site of the Rh/Cu(111) surface are displayed after reaching the thermal equilibrium at 500 K (Figure 5a-c). For H*, it tends to localize near the Cu-Pt-Cu hollow sites (Figure S4, a1-a3). For CH₃*, it prefers both the Rh top site and the adjacent hollow sites, which is attributed to the similar adsorption energies in these configurations (Figure S4, b1-b4). For the H* and CH₃* co-adsorption, they occupy the opposite Cu-Pt-Cu hollow sites, in agreement with the stable adsorption configurations at the hollow sites (Figure S4, c1-c4).

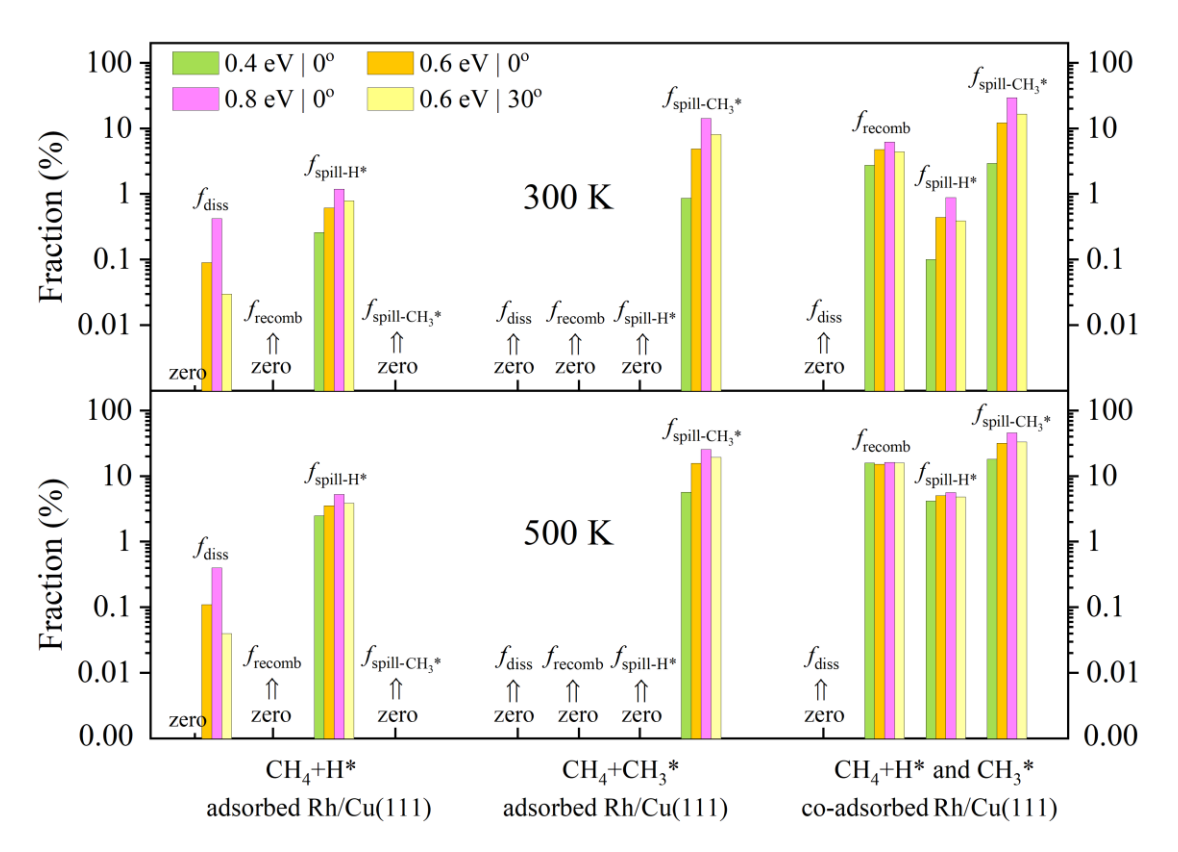


Figure **4.** Fractions of CH₄ dissociation (f_{diss}), CH₄ recombination (f_{recomb}), H* spillover ($f_{spill-H*}$) and CH₃* spillover ($f_{spill-CH_3*}$) resulting from CH₄ collisions on the fragments adsorbed Rh/Cu(111) surfaces. The values were obtained through QCT-EF calculations with different incident energies (E_i) and incident angles (θ_i) at the surface temperatures of 300 and 500 K.

As shown in Figure 4, at the surface temperature of 300 K, when CH₄ impacts on the H* adsorbed Rh/Cu(111) surface with normal incidence, the fractions of CH₄ dissociation remain remarkably low, ranging from no dissociation to 0.42 %, even when the incident energy is increased from 0.4 to 0.8 eV. This indicates that the Rh active site is partially deactivated upon H* adsorption. However, the fractions of H* spillover are significantly higher, varying from 0.26 to 1.19 % as the incident energy increases from 0.4 to 0.8 eV, indicating that the collision is the driving force to significantly promote H spillover. At the oblique angle of 30°, there is a slight increase (from 0.61 to 0.79 %)

in the fraction of H* spillover, while the fraction of CH₄ dissociation experiences a decrease (from 0.09 to 0.03 %) compared to normal incidence.

In the case of CH₄ impinging on the CH₃* adsorbed Rh/Cu(111) surface, no CH₄ dissociation is observed at the different incident energies and angles. CH₃* adsorption on the Rh site apparently also leads to its complete poisoning. This observation and the one associated with H*-poisoning of the Rh site suggest that the removal of the dissociation product is a prerequisite to keep the Rh site active for further CH₄ dissociation. Interestingly, the fractions of CH₃* spillover are significantly higher than that of H* spillover. When CH₄ is impinged on the H* and CH₃* co-adsorbed Rh/Cu(111) surface, no CH₄ dissociation is observed. Nevertheless, the collisions can still enhance H* or CH₃* spillover and also promote CH₄ recombination, with the odds of these three reaction channels being CH₃* spillover > CH₄ recombination > H* spillover.

At the surface temperature of 500 K, as shown in Figure 4, the fractions of H* or CH₃* spillover exhibit a substantial increase compared to those at 300 K. This indicates that the synergistic effect of surface temperature and gaseous molecular collisions can further enhance the spillover processes. Meanwhile, the fractions of CH₄ recombination increase with increasing surface temperature, but show minimal variation with increasing incident energy. The H* and CH₃* spillover channels become more favorable at higher temperatures with increasing incident energy.

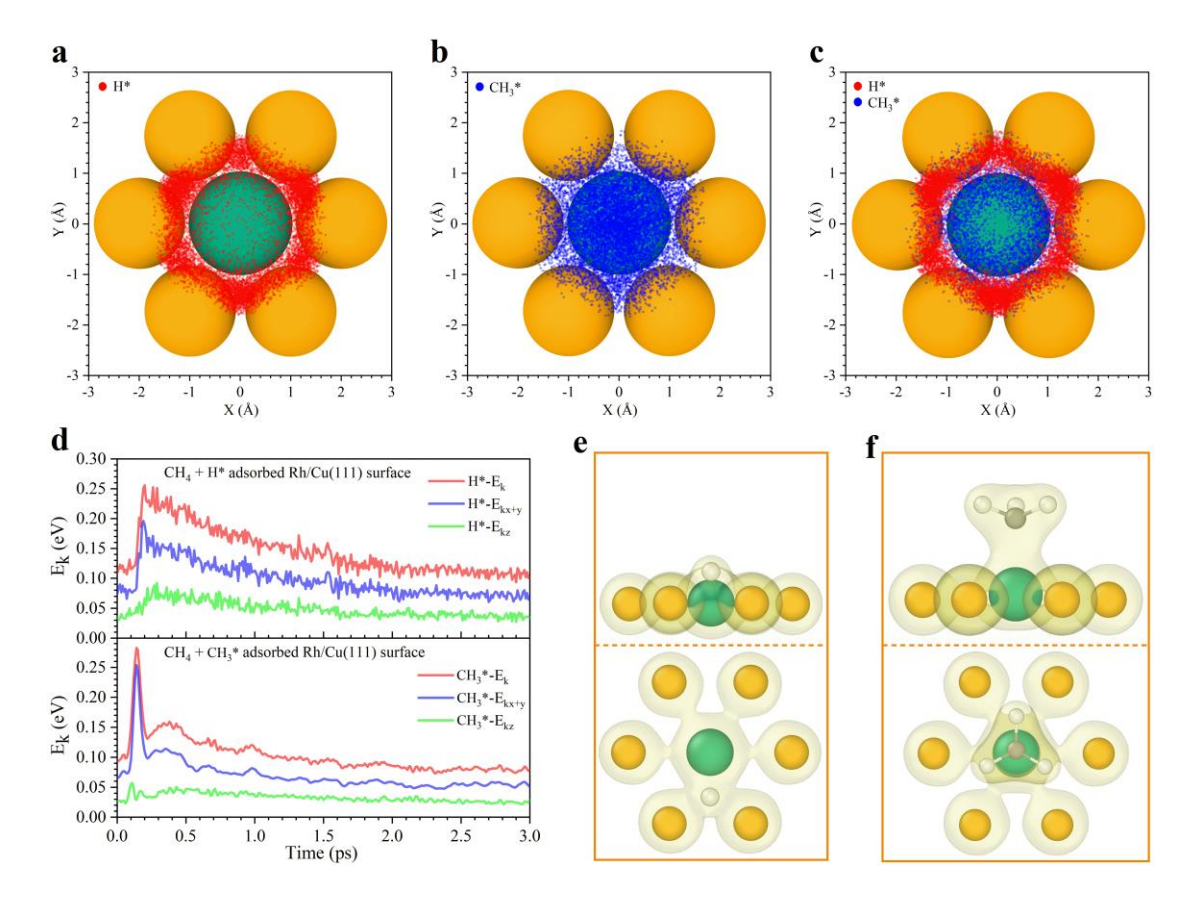


Figure 5. Dynamic characteristics of H* and CH₃* spillover on the Rh/Cu(111) surface assisted by CH₄ molecular collisions at the surface temperature of 500 K. (a, b and c) The positions of H*, CH₃*, co-adsorbed H* and CH₃* on the Rh site for the CH₄+H* adsorbed Rh/Cu(111), the CH₄+CH₃* adsorbed Rh/Cu(111) and the CH₄+(H* and CH₃*) co-adsorbed Rh/Cu(111) surfaces, respectively. The positions were obtained from a sampling of 10^4 configurations for each case. (d) The mean kinetic energy (E_k) and the corresponding kinetic energy components along x+y (E_{kx+y}) and z (E_{kz}) directions of the spilled H* or CH₃* as a function of time for all trajectories undergoing spillover. (e and f) The charge density iso-surfaces of the H* adsorbed Rh/Cu(111) surface (e) and the CH₃* adsorbed Rh/Cu(111) surface (f).

To further understand the mechanisms underlying the collision-induced spillover, we analyzed the impact of the impinging molecule on the mean kinetic energy (E_k) and the corresponding components of the adsorbed species $(H^* \text{ or } CH_3^*)$ along the surface plane (E_{kx+y}) and surface normal (E_{kz}) as a function of time. These energies are plotted

in Figure 5d as a function of time. After reaching thermal equilibrium with the surface, the E_{kx+y} of H^* or CH_3^* remains below 0.1 eV within the 0 to 100 fs time frame, which is insufficient to overcome the diffusion barriers (Figures S5 and S6). Upon collisions with CH_4 , on the other hand, E_{kx+y} of H^* or CH_3^* rapidly increase, allowing the H^* or CH_3^* to escape from the Rh site to the nearby host Cu sites. This highlights the energy transfer mechanism behind the collision-induced spillover, where the impinging CH_4 provides the adsorbed species with additional energy to overcome the corresponding diffusion barriers. Several movies are provided in the Supporting Information (Movies S1-S4) to visually illustrate the collision-induced spillover dynamics.

To understand the larger effect of collisions on the CH₃* spillover, we presented the charge density distributions of the adsorbed H* and CH₃* on the Rh/Cu(111) surface. As depicted in Figure 5e and f, the charge density of H is a small sphere, while the charge density distribution of CH₃* is more extensive, resulting in CH₃* having a larger collision cross section than H*. Consequently, although H* and CH₃* have similar spillover barriers, the larger size of CH₃* makes it more conducive to energy transfer during collisions, rendering it more susceptible to spillover than H*.

Conclusions

In this work, we leveraged machine learning to construct a first-principles based high-dimensional PES for the CH₄ collision, dissociation, and H* and CH₃* spillover processes. This PES is trained to handle four systems, namely CH₄ + Rh/Cu(111), CH₄ + H*@ Rh/Cu(111), CH₄ + CH₃*@Rh/Cu(111), and CH₄ + (H* + CH₃*)@Rh/Cu(111). Thanks to the high efficiency of the PES, we performed extensive QCT and QCT-EF

calculations to explore the spillover of the dissociated H* and CH₃* and factors that influence the spillover processes. Our results indicate that the initial spillover of the H* and CH₃* species is competitive, typically with only one escaping the dissociation site. The remaining adsorbate at the Rh site may poison the active site of the catalyst. However, the probabilities for spillover were found to be small, due to the relatively high barriers to escape from the active site. While the surface phonons promote the diffusion, the surface EHPs significantly slow the diffusion down. Interestingly, the simulations show that the pseudo-rotational mode of CH₃* exhibits a strong coupling with the reaction coordinate governing CH₃* diffusion on the host Cu(111) surface, imparting a distinct directional preference to its motion, in stark contrast to the random walk diffusion of H*. Despite an increase in surface temperature, the dissociated H* and CH₃* tend to undergo recombinative desorption forming a gaseous CH₄ molecule rather than spillover when an impinging CH₄ dissociates at the Rh site. We further demonstrate that under ambient-pressure conditions, the collision of gaseous CH₄ molecules promotes spillover of both species, due to energy transfer. This collision process might provide an effective means to reactivate the single atom site. Since the CH₃* species has a large size, its collision induced enhancement is larger than the smaller H*. These atomistic insights help to understand a key aspect of heterogeneous catalysis, which has not been extensively explored and understood.

Acknowledgments

We thank the National Natural Science Foundation of China (Grant No. 22373017 to SL) and the "Chuying Program" for the Top Young Talents of Fujian Province (SL).

HG acknowledges support from US National Science Foundation (Grant Nos. CHE-1951328 and CHE-2306975 to HG) and several useful discussions with Prof. Art Utz. We also thank Prof. Bin Jiang for helping with the PES fitting. The computations were performed at the Hefei Advanced Computing Center and the Supercomputing Center of Fujian.

Conflict of interest

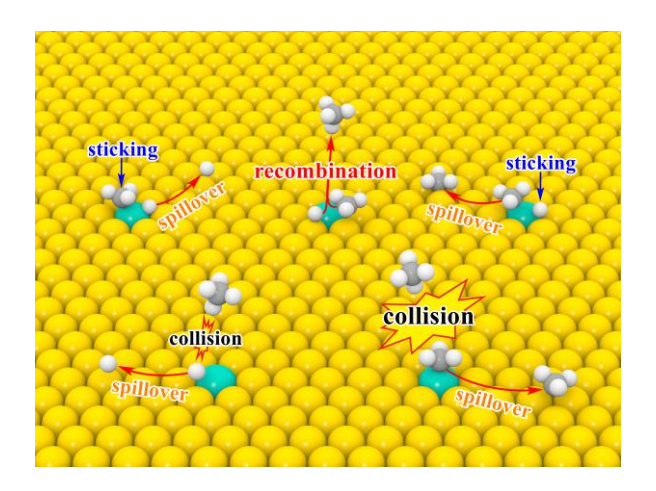
The authors declare no conflict of interest.

References

- [1] a) M. T. Darby, M. Stamatakis, A. Michaelides, E. C. H. Sykes, *J. Phys. Chem. Lett.* **2018**, *9*, 5636-5646; b) R. T. Hannagan, G. Giannakakis, M. Flytzani-Stephanopoulos, E. C. H. Sykes, *Chem. Rev.* **2020**, *120*, 12044-12088.
- [2] a) T. Zhang, A. G. Walsh, J. Yu, P. Zhang, *Chem. Soc. Rev.* 2021, 50, 569-588;
 b) T. Shen, S. Wang, T. Zhao, Y. Hu, D. Wang, *Adv. Energy Mater.* 2022, 12, 2201823.
- a) H. L. Tierney, A. E. Baber, J. R. Kitchin, E. C. H. Sykes, *Phys. Rev. Lett.* 2009, 103, 246102; b) A. E. Baber, H. L. Tierney, T. J. Lawton, E. C. H. Sykes, *ChemCatChem* 2011, 3, 607-614; c) G. Kyriakou, M. B. Boucher, A. D. Jewell, E. A. Lewis, T. J. Lawton, A. E. Baber, H. L. Tierney, M. Flytzani-Stephanopoulos, E. C. H. Sykes, *Science* 2012, 335, 1209-1212; d) M. D. Marcinkowski, A. D. Jewell, M. Stamatakis, M. B. Boucher, E. A. Lewis, C. J. Murphy, G. Kyriakou, E. C. H. Sykes, *Nat. Mat.* 2013, 12, 523-528; e) E. A. Lewis, M. D. Marcinkowski, C. J. Murphy, M. L. Liriano, E. C. H. Sykes, *J. Phys. Chem. Lett.* 2014, 5, 3380-3385; f) F. R. Lucci, M. D. Marcinkowski, T. J. Lawton, E. C. H. Sykes, *J. Phys. Chem. C* 2015, 119, 24351-24357.
- a) F. R. Lucci, J. Liu, M. D. Marcinkowski, M. Yang, L. F. Allard, M. Flytzani-Stephanopoulos, E. C. Sykes, *Nat. Commun.* **2015**, *6*, 8550; b) M. D. Marcinkowski, M. T. Darby, J. Liu, J. M. Wimble, F. R. Lucci, S. Lee, A. Michaelides, M. Flytzani-Stephanopoulos, M. Stamatakis, E. C. H. Sykes, *Nat. Chem.* **2018**, *10*, 325-332; c) R. Réocreux, P. L. Kress, R. T. Hannagan, V. Çınar, M. Stamatakis, E. C. H. Sykes, *J. Phys. Chem. Lett.* **2020**, *11*, 8751-8757; d) R. T. Hannagan, G. Giannakakis, R. Réocreux, J. Schumann, J. Finzel, Y. Wang, A. Michaelides, P. Deshlahra, P. Christopher, M. Flytzani-Stephanopoulos, M. Stamatakis, E. C. H. Sykes, *Science* **2021**, *372*, 1444-1447.
- [5] R. Prins, Chem. Rev. 2012, 112, 2714-2738.

- [6] a) J. Liu, F. R. Lucci, M. Yang, S. Lee, M. D. Marcinkowski, A. J. Therrien, C. T. Williams, E. C. H. Sykes, M. Flytzani-Stephanopoulos, J. Am. Chem. Soc. 2016, 138, 6396-6399; b) R. Réocreux, E. C. H. Sykes, A. Michaelides, M. Stamatakis, J. Phys. Chem. Lett. 2022, 13, 7314-7319; c) R. T. Hannagan, H. Y. Lam, R. Réocreux, Y. Wang, A. Dunbar, V. Lal, V. Çınar, Y. Chen, P. Deshlahra, M. Stamatakis, N. M. Eagan, E. C. H. Sykes, J. Phys. Chem. Lett. 2023, 14, 10561-10569.
- [7] C. R. O'Connor, K. Duanmu, D. A. Patel, E. Muramoto, M. A. van Spronsen, D. Stacchiola, E. C. H. Sykes, P. Sautet, R. J. Madix, C. M. Friend, *Proc. Natl. Acad. Sci. U. S. A.* 2020, 117, 22657-22664.
- [8] G.-C. Zhao, Y.-Q. Qiu, C.-G. Liu, Appl. Catal. A 2021, 610, 117948.
- [9] a) M. Ramos, A. E. Martínez, H. F. Busnengo, *Phys. Chem. Chem. Phys.* 2012, 14, 303-310; b) J. Meyer, K. Reuter, *Angew. Chem. Int. Ed.* 2014, 53, 4721-4724; c) K. Gu, F. Wei, Y. Cai, S. Lin, H. Guo, *J. Phys. Chem. Lett.* 2021, 12, 8423-8429; d) K. Gu, C. Li, B. Jiang, S. Lin, H. Guo, *J. Phys. Chem. C* 2022, 126, 17093-17101; e) Y. Wang, H. Guo, *J. Phys. Chem. C* 2023, 127, 4079-4086; f) K. Gu, S. Lin, H. Guo, *J. Phys. Chem. C* 2023, 127, 21568-21577; g) Q. Lin, B. Jiang, *J. Phys. Chem. Lett.* 2023, 14, 7513-7518.
- [10] K. Gu, S. Lin, Angew. Chem. Int. Ed. 2023, 62, e202312796.
- [11] B. Jiang, H. Guo, J. Chem. Phys. **2019**, 150, 180901.
- [12] a) J. Behler, Angew. Chem. Int. Ed. 2017, 56, 12828-12840; b) B. Jiang, J. Li,
 H. Guo, J. Phys. Chem. Lett. 2020, 11, 5120-5131.
- [13] a) W. Fang, J. O. Richardson, J. Chen, X.-Z. Li, A. Michaelides, *Phys. Rev. Lett.* 2017, 119, 126001; b) L. Kristinsdóttir, E. Skúlason, *Surf. Sci.* 2012, 606, 1400-1404.
- [14] L. Xu, J. Lin, Y. Bai, M. Mavrikakis, *Top. Catal.* **2018**, *61*, 736-750.
- [15] J. Juaristi, M. Alducin, R. D. Muiño, H. F. Busnengo, A. Salin, *Phys. Rev. Lett.* **2008**, *100*, 116102.
- [16] X. Luo, B. Jiang, J. I. Juaristi, M. Alducin, H. Guo, *J. Chem. Phys.* **2016**, *145*, 044704.
- [17] M. P. Allen, D. J. Tildesley, *Computer simulation of liquids*, Oxford university press, **2017**.
- [18] H. Guo, B. Jiang, Acc. Chem. Res. 2014, 47, 3679-3685.
- [19] a) G. X. Cao, E. Nabighian, X. D. Zhu, *Phys. Rev. Lett.* 1997, 79, 3696-3699; b)
 T. Firmino, R. Marquardt, F. Gatti, W. Dong, *J. Phys. Chem. Lett.* 2014, 5, 4270-4274.

TOC Graphic



Sentence for TOC graphics:

Under real-world conditions, the frequent collisions of gaseous CH₄ molecules on Rh/Cu(111) single-atom alloy are a key to promote adsorbate spillover, especially for bulky polyatomic CH₃* species, providing insights into the effective use of spillover in heterogeneous catalysis.